Journal of Molecular Structure 1299 (2024) 137127

Contents lists available at ScienceDirect

Journal of Molecular Structure

journal homepage: www.elsevier.com/locate/molstr

A study on the impact of $[BO_3^{3-}]$, $[PO_4^{3-}]$ and $[SO_4^{2-}]$ ions in normal cubic structures via structural and photoluminescence properties of Y_2O_3: Eu^{3+} phosphors

T.G. Mathe [a], A. Balakrishna [a,*], M.A. Mamo [b], O.M. Ntwaeaborwa [c], R.E. Kroon [d], E. Coetsee [d], H. C. Swart [d], L. Reddy [a,*]

[a] Department of Physics, University of Johannesburg, Johannesburg ZA-2006, South Africa
[b] Department of Chemical Sciences, University of Johannesburg, Johannesburg ZA-2006, South Africa
[c] School of Physics, University of the Witwatersrand, Wits, Johannesburg 2050, South Africa
[d] Department of Physics, University of the Free State, Bloemfontein ZA-9300, South Africa

ARTICLE INFO

Keywords:
Y_2O_3:Eu^{3+} phosphors
PO_4^{3-}, SO_4^{2-} and BO_3^{3-} ions
Photoluminescence CIE color coordinates

ABSTRACT

A series of Y_2O_3-AG: Eu^{3+} (where AG = Anionic Groups [PO_4^{3-}, SO_4^{2-} and BO_3^{3-}]) nanophosphors were synthesized via a chemical combustion method and their structural and photoluminescence properties were investigated. The crystal structure and the surface morphology studies were analysed through the X-Ray powder diffraction (XRPD), Field-emission scanning electron microscopy (FE-SEM), Fourier-transform infrared spectroscopy (FT-IR) and X-ray photoelectron spectroscopy (XPS). The XRD results showed that undoped Y_2O_3 phosphors crystalized in a cubic crystal structure, while the Y_2O_3-AG phosphors transformed from the pure Y_2O_3 cubic structures, except for SO_4^{2-} based phosphor materials. The SEM micrographs showed that the particles were formed in the micrometer range with different sizes and shapes. The FTIR spectra revealed the presence of various structural groups in the Y_2O_3, Y_2O_3-AG: Eu^{3+} phosphors. Moreover, the optical diffuse reflectance spectroscopy (DRS) and photoluminescence (PL) properties were investigated. Using the DRS data, the optical band gap energy values were obtained from the Kubelka-Munk function theory. Upon 395 nm excitation, the Y_2O_3-AG: Eu^{3+} phosphors emitted red light at 615 nm wavelength. Among all the samples, the Y_2O_3-BO_3: Eu^{3+} produced the highest intensity of red-light emission. The International Commission on Illumination color coordinates indicated that these phosphors are potential candidates for producing enhanced red color components in white light-emitting diode (W-LEDs) applications.

1. Introduction

Nowadays, white light emitting diodes (W-LEDs) are the next generation of solid-state lighting due to their superior properties such as cost-effectiveness, easy preparation, environmental friendly, high luminescence efficiencies and longer lifetime [1–4]. The general structure to fabricate W-LEDs is mainly through the combination of a blend of red, green, and blue colours that are produced by different phosphor materials when they are excited by a near-ultraviolet light source [5,6]. The cubic structure model of Y_2O_3 with a body-centered positions of the Y^{3+} ions in the middle of the cubic lattice, while the oxygen ions (O^{2-}) are located at the corners of the cubic lattice [7,8]. Choosing a simple cubic structure model has the advantage of making it easy to track structural changes through the introduction of various anionic groups or dopant ions into the cubic lattices [9]. In light of this, the impact of anionic group substitutional effect of ionic group substitutions plays a crucial role in enhancing absorption properties of Y_2O_3 materials [10]. In this respect, the anionic group systems are chosen from the chemical compounds for substitution into the Y_2O_3 materials [11,12]. For example, Yousif et al., reported the structural and luminescence properties of Y_2O_3 red phosphor by incorporation of Ga^{3+} and Bi^{3+}ions [13]. R.S. Ukare et al. studied the effect of Li^+ and Zn^{2+} co-doping on PL properties of Y_2O_3 phosphors [14]. Danmian Wang et al. reported emission of white light from YVO_4/Y_2O_3 composite phosphors for UV light-emitting diodes application [15]. In the periodic table lanthanides ions play a crucial role in the field of solid-state lighting applications. In

* Corresponding authors.
E-mail addresses: bavula@uj.ac.za (A. Balakrishna), krishr@uj.ac.za (L. Reddy).

https://doi.org/10.1016/j.molstruc.2023.137127
Received 22 September 2023; Received in revised form 12 November 2023; Accepted 19 November 2023
Available online 20 November 2023

this case, rare earth ions are responsible for producing respective emission colours of visible light when doped in various host materials [16]. Among all different rare earth ions, europium ions (Eu^{3+}) in any host materials are responsible for the characteristic red-light emissions, around 614 nm wavelength, which is attributed to the $^5D_0 \rightarrow {}^7F_2$ transitions [17]. Up to now, many researchers have reported on the red emission of Y_2O_3:Eu^{3+} phosphor materials with a poor color rendering index (CRI). To address this issue, the anionic group systems such as PO_4^{3-}, SO_4^{2-} and BO_3^{3-} were introduced to the Y_2O_3 matrices to enhance the Eu^{3+} red color emission, thereby improving its CRI index [18–20].

In this work, we synthesized Y_2O_3, Y_2O_3-AG: Eu^{3+} where AG = PO_4^{3-}, SO_4^{2-}, BO_3^{3-}) nanophosphors, via the chemical combustion method. The structural and morphological properties of these materials were characterized to investigate their crystal structure and particle morphology. In addition to this, the optical and photoluminescence properties were also investigated. In this present work, the impact of the anionic groups on the red color emission of Y_2O_3:Eu^{3+} phosphors were examined.

2. Experimental techniques

In this study, Y_2O_3, Y_2O_3-AG: Eu^{3+} nanophosphors were prepared using a chemical combustion method. The samples were annealed at 1100 °C for 4 h. In this method, the raw materials were yttrium nitrate, ammonium dihydrogen sulfate, boric acid ammonium phosphate, urea and europium nitrate. The 1 mol% of europium ions were doped into the Y_2O_3, Y_2O_3-AG compounds. The raw materials were mixed in one beaker and then dissolved in de-ionized water and then placed over a magnetic stirrer for a period of 45 min. The final solution was then placed in a porcelain crucible and then transferred to the furnace that was pre-heated to 600 °C for a minimum duration of 10–15 min. The product was removed from the furnace and again ground into a fine powder using a mortar and pestle. The basic balanced equation for the preparation of Y_2O_3 is:

$$2\ Y(NO_3)_3 + 15\ NH_2CONH_2 \rightarrow Y_2O_3 + 18\ N_2 + 15\ CO_2 + 30\ H_2$$

Various characterization techniques were used to analyze the samples, namely, X-ray powder diffraction (XRD), scanning electron microscopy (SEM) equipped with an energy dispersive X-ray spectroscope (EDS), Fourier Transformed Infra-red spectroscopy (FTIR), diffuse reflectance spectroscopy (DRS), and photoluminescence (PL) spectroscopy. Philips X'Pert Pro-X-Ray Diffractometer coupled with PANalytical software was used to evaluate the crystal structure. A nickel-filtered CuKα target were used with the wavelength target set at 0.1540 nm. Philips CM100 Mega View III field emission scanning electron microscope (FE-SEM), coupled with the Oxford Aztec 350 X-Max80 EDS was used to obtain the surface morphology and chemical composition of the prepared materials. FTIR spectra were measured using the Shimadzu QATR 10 single reflection ATR accessory, which were recorded from 400 cm^{-1} to 4000 cm^{-1}. The chemical composition and electronic states were analyzed using the PHI 5000 Scanning ESCA Versaprobe X-ray photoelectron spectroscope. The optical reflection spectra were recorded at room temperature using the PerkinElmer Lambda 900 spectrophotometer, in the range of 250–2300 nm. For photoluminescence studies, the Cary eclipse fluorescence spectrophotometer was used at room temperature with a monochromatized 150 W xenon lamp as excitation source. The lifetime decay measurements were taken using FS5 spectrofluorometer from Edinburgh Instruments. The quantum yield measurements were done by using the Edinburgh Instruments FLS980 instrument equipped with an integrating sphere.

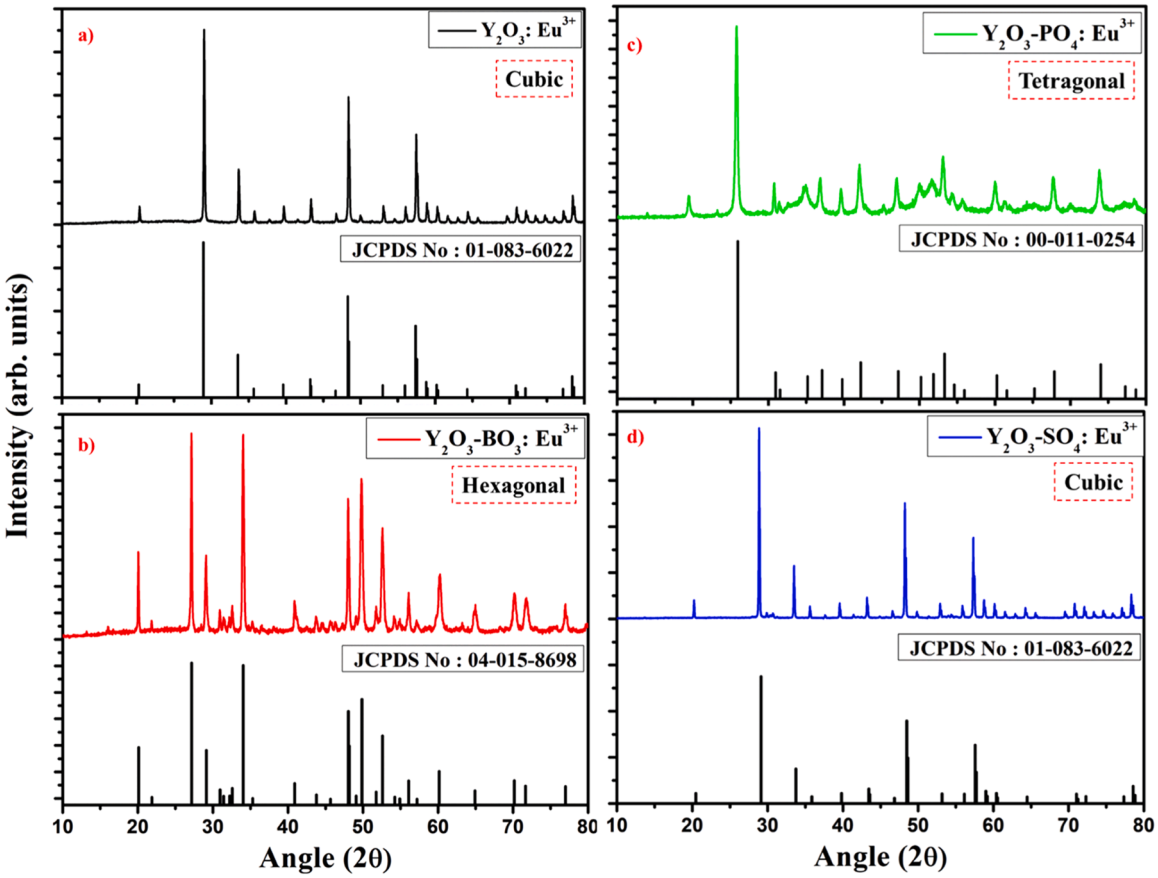

Fig. 1. The full XRPD patterns of (a)Y_2O_3: Eu^{3+}, (b) Y_2O_3-BO_3: Eu^{3+}, (c)Y_2O_3-PO_4: Eu^{3+} and (d)Y_2O_3-SO_4: Eu^{3+}phosphors.

3. Results and discussion

3.1. X-ray diffraction analysis

Fig. 1. shows the X-ray powder diffraction (XRPD) patterns of Y_2O_3, Y_2O_3-AG: Eu^{3+}nanophosphors. All X-ray diffraction patterns showed that these materials were formed into cubic lattice structures, which matched well with the background pattern of the Y_2O_3 structure with JCPDS file no. 86–1326, which is also displayed in Fig. 1. The XRPD reflection peaks of pure Y_2O_3 are located at 2θ angles of 20.26°, 29.17°, 33.74°, 35.73°, 39.81°, 43.52°, 48.24°, 52.94° and 57.26° which correspond to the lattice planes of (2 1 1) (2 2 2) (4 0 0) (4 1 1) (3 2 2) (4 3 1) (4 4 0) (6 1 1) (6 2 2) respectively [21]. The lattice structure parameters of Y_2O_3 is $a = b = c = 10.759$ Å [21–23]. The addition of Eu^{3+} to Y_2O_3 resulted in no significant changes in the diffraction patterns, however substitution of different anionic systems resulted in changes in the crystal structures from cubic to hexagonal for the Y_2O_3-BO_3 (JCPDS file no. 04–015–8698) and cubic to tetragonal for the Y_2O_3-PO_4 (JCPDS file no. 00–011–0254) and no changes for the SO_4 based phosphors. Substitution of anionic group systems (AG = BO_3^{3-} and PO_4^{3-}), created the possibility of structural deformation in Y_2O_3 lattices. This is because of the compressive strain created in the lattice, due to the BO_3^{3-} and PO_4^{3-} ions substitution [24]. Fig. 2 displays the Williamson-Hall (W-H) plots for the Y_2O_3:Eu^{3+}, Y_2O_3-AG: Eu^{3+}nanophosphors. The linear fitting of the W-H plots reveals parameters such as crystalline size and lattice strain values obtained through the slope and Y-intercept of the linear plot. The negative slope of the W-H plots indicates a compressive strain for all the Y_2O_3:Eu^{3+} and Y_2O_3-AG: Eu^{3+}phosphors due to lattice shrinkage [25]. Table 1 shows the crystalline size and lattice strain values calculated through the Scherrer formulae and W-H method, respectively [25]. The calculated crystallite sizes for these prepared materials were found in the range of 20–73 nm, as presented in Table 1.

Table 1
Crystallite size of the Y_2O_3: Eu^{3+}, Y_2O_3-BO_3: Eu^{3+}, Y_2O_3-PO_4: Eu^{3+} and Y_2O_3-SO_4: Eu^{3+} phosphors.

S. No	Sample	Crystallite size (nm)		Strain (x10^{-3})
		Scherrer	W-H plot	
1	Y_2O_3:Eu^{3+}	68	90	−3
2	Y_2O_3-BO_3:Eu^{3+}	51	98	−2.2
3	Y_2O_3-PO_4:Eu^{3+}	20	89	−1.5
4	Y_2O_3-SO_4:Eu^{3+}	73	95	−4

These particle size values were compared to the values obtained from the W-H plots. Both methods show a good agreement of the particle size values of the prepared phosphors, in the range of ~60 nm. It is also observed from the table that the addition of anionic group systems leads to random changes in the crystallite particle sizes, such as 51 nm for Y_2O_3-BO_3^{3-}: Eu^{3+}, 20 nm for Y_2O_3- PO_4^{2-}: Eu^{3+}, and 73 nm for Y_2O_3-SO_4^{2-}: Eu^{3+}. From the table, it is also observed that the lattice strain values were increased for the BO_3^{3-} and PO_4^{3-} ions-based compounds, which confirms the deformation of cubic Y_2O_3 structures to the new type of hexahedral and tetrahedral structures for Y_2O_3-BO_3 and Y_2O_3-PO_4 phosphors, respectively.

Rietveld refinement structural parameters of the Y_2O_3, Y_2O_3-AG: Eu^{3+} nanophosphors were determined using the Full-Prof suite. Rietveld profile fits well for all the XRD patterns of Y_2O_3, Y_2O_3-AG: Eu^{3+} nanophosphors after refinement, as shown in Figs. 3 (a-f). Analysis of the fit reveals that there is close co-relation between the observed and calculated XRPD patterns. In this figure, the solid lines dots represent the measured experimental XRPD data, while the red color solid line represents the theoretical XRPD data patterns. However, the difference between these two data points is represented by purple solid line in the Figure. The additional vertical bars show the Bragg's positions of the respective XRPD patterns of the materials. Results obtained from the

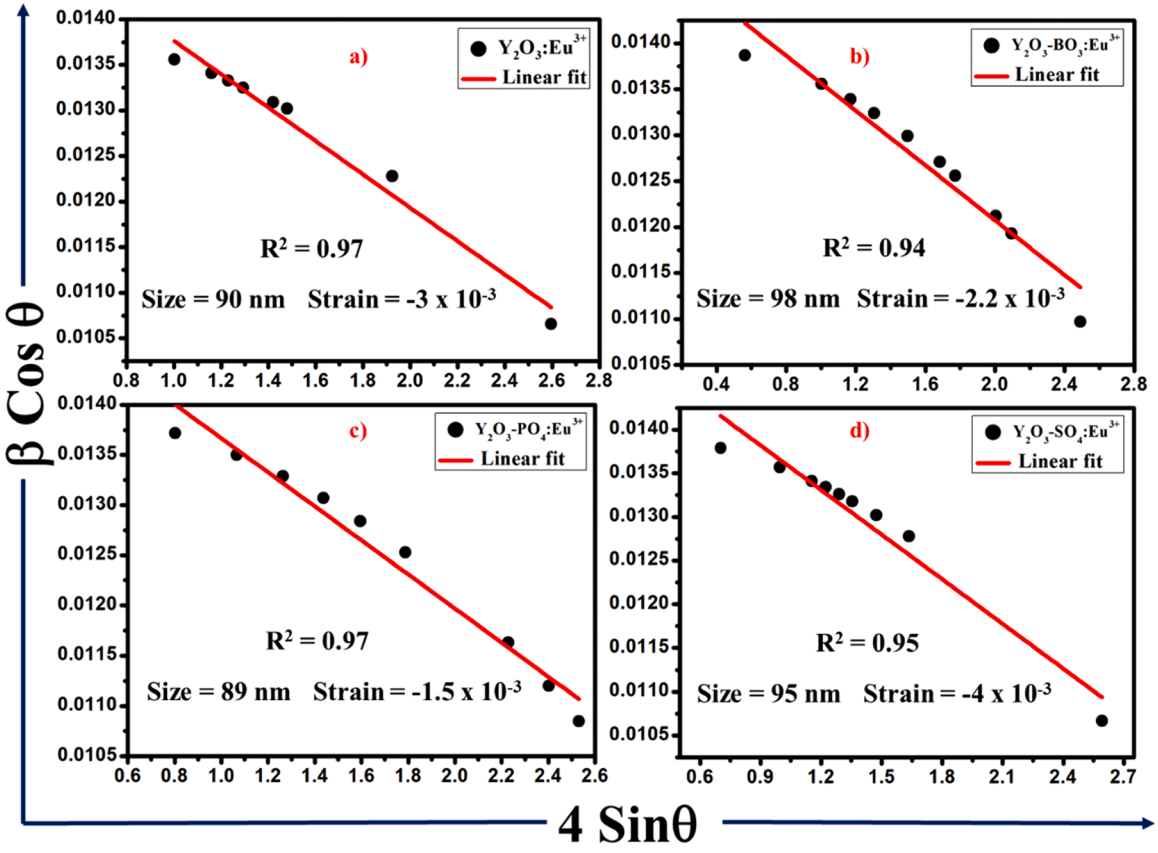

Fig 2. The W-H plots of (a)Y_2O_3: Eu^{3+}, (b) Y_2O_3-BO_3: Eu^{3+}, (c)Y_2O_3-PO_4: Eu^{3+} and (d)Y_2O_3-SO_4: Eu^{3+}phosphors.

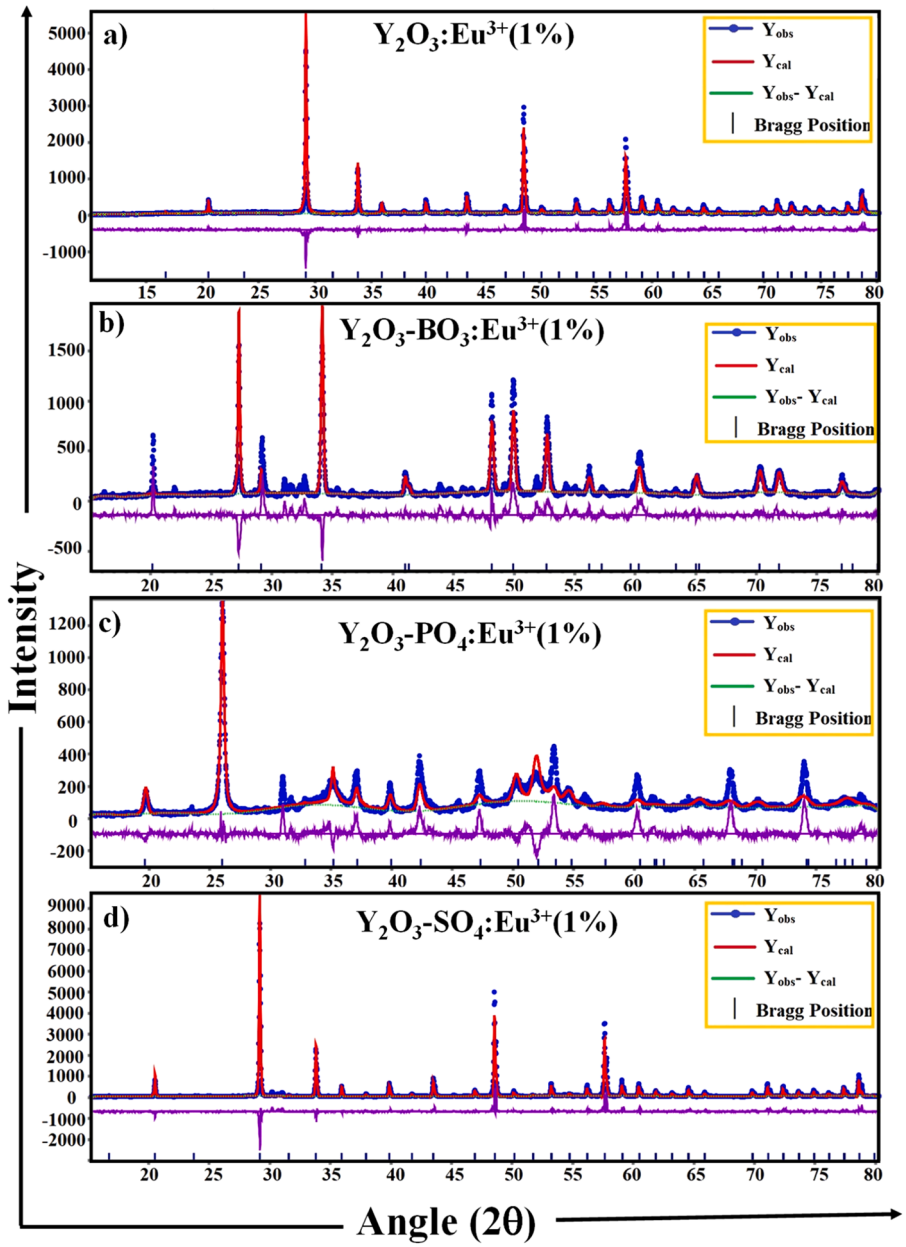

Fig. 3. Rietveld analysis of different (a)Y_2O_3: Eu^{3+}, (b) Y_2O_3-BO_3: Eu^{3+}, (c)Y_2O_3-PO_4: Eu^{3+} and (d)Y_2O_3-SO_4: Eu^{3+} phosphors.

Rietveld refinement analysis of prepared nanophosphors are presented in Table 2. This table consists of refinement agreement factors, lattice parameters along with the cell volume values of all studied materials. From the table, it is observed that the lattice parameters of all materials were found to be very close to the calculated standard data of the respective crystalline materials. Fig. 4 displayed the unit cell structure of all Y_2O_3, Y_2O_3-AG: Eu^{3+} nanophosphors. The cell volume of the Y_2O_3 phosphors is also in good agreement with the standard data for this material. However, when BO_3^{3-} and PO_4^{3-} anions added into Y_2O_3 materials reduced the volume of the unit cells, indicating that the cubic structures of the Y_2O_3 were transformed to the new crystalline structures via the replacement of BO_3^{3-} and PO_4^{3-} anions within the Y_2O_3 cubic lattice. However, no such changes in the cell volume of Y_2O_3-SO_4 materials, which indicates that SO_4^{2-} ions were positioned into the interstitial sites of the Y_2O_3 cubic lattices resulting in no crystalline deformation as also shown in XRPD diffraction patterns of Fig. 1. The chemical features of all compounds are summarized in Table 3.

For the compound, Y_2O_3, when the coordination number (CN) is 6, implies that Y is surrounded by 6 O atoms or *vice versa*. In this scenario,

Table 2
The lattice parameters, unit cell volume, goodness of fit, and R-factors of Y_2O_3: Eu^{3+}, Y_2O_3-BO_3: Eu^{3+}, Y_2O_3-PO_4: Eu^{3+} and Y_2O_3-SO_4: Eu^{3+} phosphors.

S. No.	Sample	R_p	R_{wp}	R_{exp}	χ^2	Lattice parameters (Å)	Cell volume $(Å)^3$
1	Y_2O_3: Eu^{3+}	14.57	18.65	9.31	4.01	$a = b = c =$ 10.59	1188.63
2	Y_2O_3-BO_3: Eu^{3+}	20.08	25.09	9.15	7.52	$a = b = 3.78$, $c = 8.80$	108.78
3	Y_2O_3-PO_4: Eu^{3+}	18.33	24.36	9.70	6.31	$a = b = 6.84$, $c = 6.00$	280.63
4	Y_2O_3-SO_4: Eu^{3+}	18.59	23.52	8.57	7.53	$a = b = c =$ 10.60	1189.57

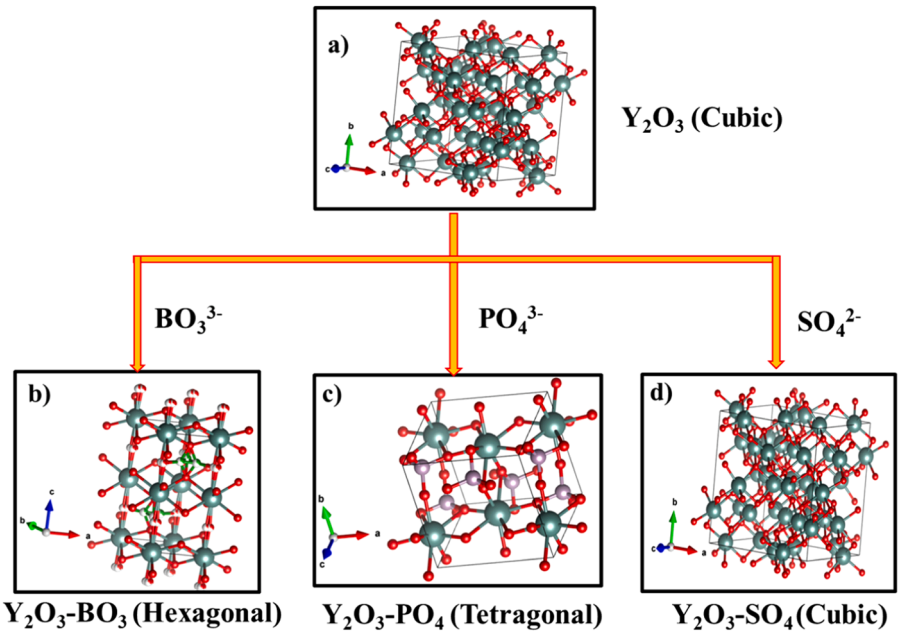

Fig. 4. Unit cell structure of different (a)Y_2O_3: Eu^{3+}, (b) Y_2O_3-BO_3: Eu^{3+}, (c)Y_2O_3-PO_4: Eu^{3+} and (d)Y_2O_3-SO_4: Eu^{3+} phosphors.

Table 3
Structural properties and bond length for Y_2O_3, Y_2O_3-AG: Eu^{3+} nanophosphors.

S. No	Compound	Space group	Crystal structure	Bond length
1	Y_2O_3:Eu^{3+}	1a-3	Cubic	Y-O (Y_1/O_1) = 2.25712 Å Y-O (Y_2/O_1) = 2.26507Å
2	Y_2O_3-BO_3/YBO_3: Eu^{3+}	P63/m mc	Hexagonal	B-O (B_1/O_2) = 1.58410 Å B-Y (B_1/Y_1) = 2.46223 Å B-O (B_1/O_1) = 1.10420 Å O-Y (O_2/Y_1) = 2.41702Å
3	Y_2O_3-PO_4/YPO_4: Eu^{3+}	141/a md:2	Tetragonal	P-O (P_1/O_1) = 1.39712 Å O-Y (O_1/Y_1) = 2.4420Å
4	Y_2O_3-SO_4:Eu^{3+}	1a-3	Cubic	Y-O (Y_1/O_1) = 2.27162 Å Y-O (Y_2/O_1) =2.24840Å

the radius of Y^{3+} ions are relatively close to the dopant Eu^{3+} ions. The relative error in% when substituting Eu^{3+}(1.17 Å) ions with Y^{3+} (1.011 Å) ions for CN = 6 or 8, using the formula below,

$$\Delta_r = \frac{|R_a\ (CN=6\ or\ 8) - R_b\ (CN=6\ or\ 8)|}{R_a} \times\ 100\% \qquad (2)$$

where R_a/R_b represents the ionic radius of dopant and original ions, respectively. The average Δ_r obtained values are ~15.7 % and ~ 4.95% for Y_2O_3, Y_2O_3-AG: Eu^{3+} nanophosphors. This percentage is less than 30 % and it means that Eu^{3+} ions have a high probability to be substituted for Y^{3+} ions, without causing any major crystal distortions to the host lattice [26,27].

3.2. Surface morphology analysis

Fig. 5 shows SEM (a,b,c,d) and EDS (e,f,g,h) images of pure Y_2O_3 and Y_2O_3-AG nanophosphors, respectively. All micrographs were captured at the same magnification level for the purposes of similar comparisons. Fig. 5(a) displays particles of different sizes and shapes with a low level of agglomeration, whereas Fig. 5(b–d) consists of spherical-like shape particles with a higher level of agglomeration, due to the addition of BO_3, PO_4 and SO_4 ions, respectively. It is also noticed from this figure; that the compact nature of the materials is high in PO_4 materials whereas it is low in SO_4 materials due to the voids created by escaping gasses during calcination [28]. Fig. 5 (e–h) displays the corresponding EDS spectra of the Y_2O_3-AG: Eu^{3+} nanophosphors, respectively. The EDS spectra confirm the presence of all elements of the respective compounds, with the dominant elements being Y and O followed by trace elements of P, B, and S for all synthesized Y_2O_3-AG nanophosphors respectively. Some trace elements of impurities such as carbon were found in the black tape used for mounting during measurements. Fig. 6 (a–h) shows the SEM and EDS images of pure Y_2O_3 and Y_2O_3-AG:Eu^{3+} nanophosphors, respectively. Fig. 6 displays comparable data for the Eu^{3+} doped nanophosphors regarding agglomeration, particle sizes, and shapes.

3.3. Fourier transform infrared spectroscopy (FT-IR)

FTIR measurements in the range of 400–4000 cm^{-1} were performed to analyze the structural groups present in the prepared phosphor materials. Fig. 7 shows the FT-IR spectra of the Y_2O_3-AG: Eu^{3+} nanophosphors. The bonds of the Y-O matrix are observed at around 430 cm^{-1} due to the vibrational properties within the Y_2O_3 [29,30]. The substitution of the anionic groups such as BO_3, PO_4 and SO_4 ions, which were measured at room temperature are observed at 850 cm^{-1}, 950 cm^{-1} and 1025 cm^{-1} respectively [24,31]. The peak observed at 1025 cm^{-1} is attributed to the presence of the BO_3 compounds [32]. The broad transmission around at 3625 cm^{-1} is attributed to the stretching modes of the O—H bonds that exist in the materials [33]. This is due to the accumulation of moisture on the surface of the samples during characterization measurements [30,33].

3.4. Surface characterization by X-ray photoelectron spectroscopy (XPS)

Fig. 8 shows the elemental composition in the XPS survey spectra of the a) Y_2O_3-BO_3 & Y_2O_3-BO_3:$Eu^{3+}$and the b) Y_2O_3-PO_4 & Y_2O_3-PO_4: Eu^{3+} phosphor materials. Fig. 8(a and b) shows the XPS peak of various

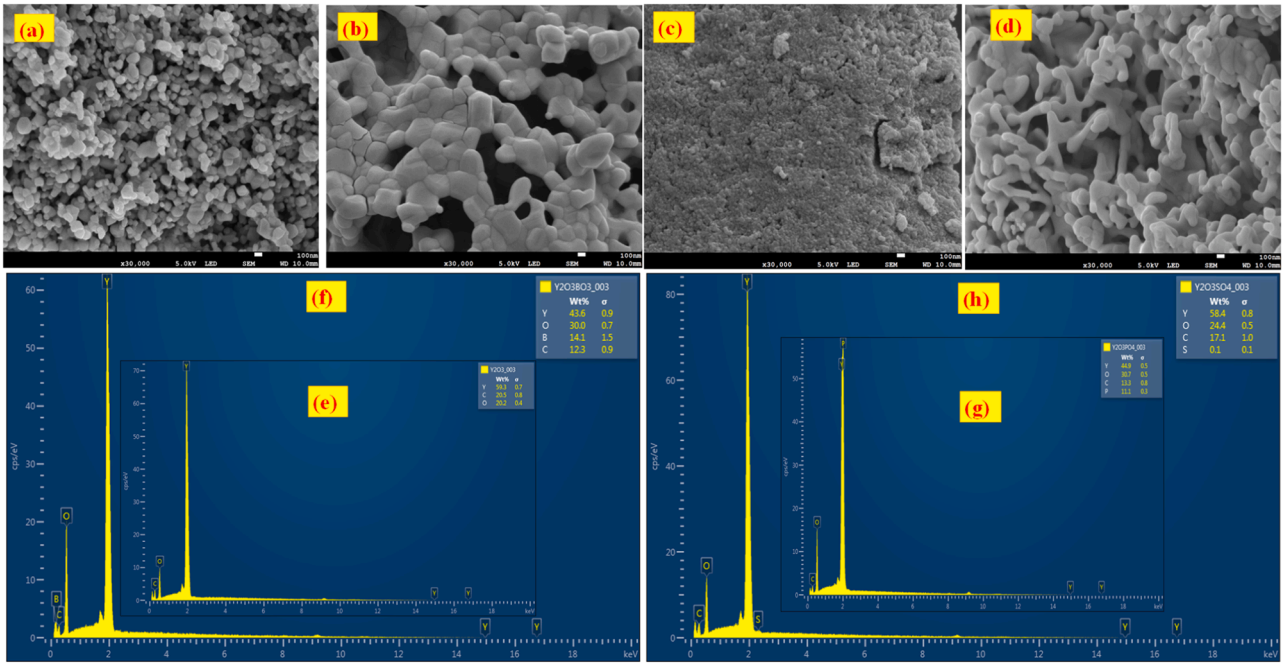

Fig. 5. SEM and EDS images of pure (a),(e)Y_2O_3 (b),(f) Y_2O_3-BO_3, (c),(g) Y_2O_3-PO_4 and (d),(h)Y_2O_3-SO_4: Eu^{3+} phosphors.

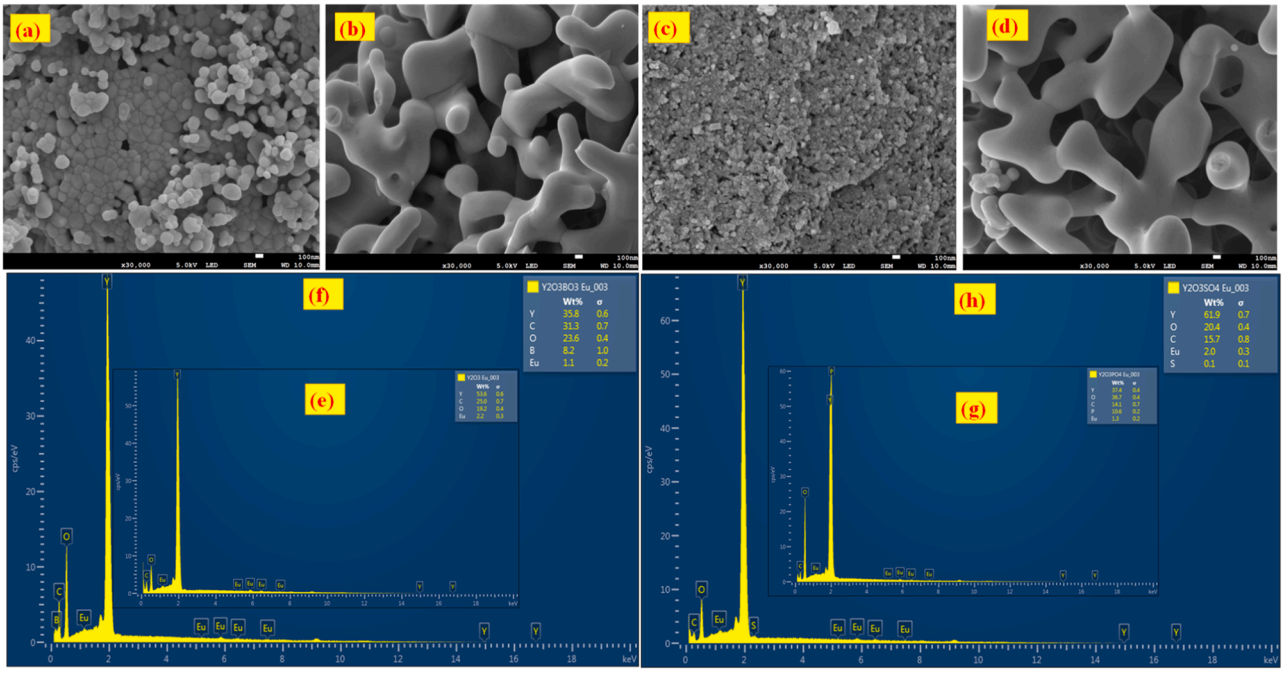

Fig. 6. SEM and EDS images of (a),(e)Y_2O_3: Eu^{3+} (b),(f) Y_2O_3-BO_3: Eu^{3+} (c),(g)Y_2O_3-PO_4: Eu^{3+} and (d),(h) Y_2O_3-SO_4: Eu^{3+} phosphors.

elements in the prepared materials above, which were identified as Y, B, P, C, O, F, and Eu signals. The survey spectra show the only difference in finding B and P peaks for the Y_2O_3-BO_3:$Eu^{3+}$and Y_2O_3-PO_4:Eu^{3+} phosphor materials, which confirms the presence of BO_3^{3-} and PO_4^{2-} groups. In addition to this, the presence of impurities such as carbon and fluorine arise from the carbon tape or from the surface contamination during measurements [34,35].

Fig. 9(a–d) shows high-resolution XPS spectra of (a) Y 3d, (b) B 1 s, (c) O 1 s and (e, f) Eu 3d of the Y_2O_3-BO_3 and Y_2O_3-BO_3:Eu^{3+} nano phosphors. The element Y 3d has a binding energy of 157.84 eV which corresponds to an oxidation state of +3 in the Y-O bonds [35]. The B 1 s peak shows a binding energy of 192.27 eV, which indicates an oxidation state of +3 [36]. Similarly, O 1 s has an oxidation state of −2 corresponding to a binding energy of 531.04 eV [37]. Furthermore, Eu 3d has an oxidation state of +3 with doublet spin-orbit coupling states of $3d_{3/2}$ and $3d_{5/2}$ corresponding to a binding energy of 1124.60 and 1154.47 eV respectively [38]. Additional peaks positioned at 1124.10 eV and 1155.24 eV binding energies are attributed to the presence of the +2 state of Eu atoms [38]. The inset figures of Fig. 9(a) and (c) shows the de-convoluted peaks of Y 3d and O 1 s bands respectively [39,40,38]. The Gaussian peaks of Y 3d indicates that doublet spin-orbit coupling states of $3d_{3/2}$ and $3d_{5/2}$ correspond to a binding energy of 159.59 eV

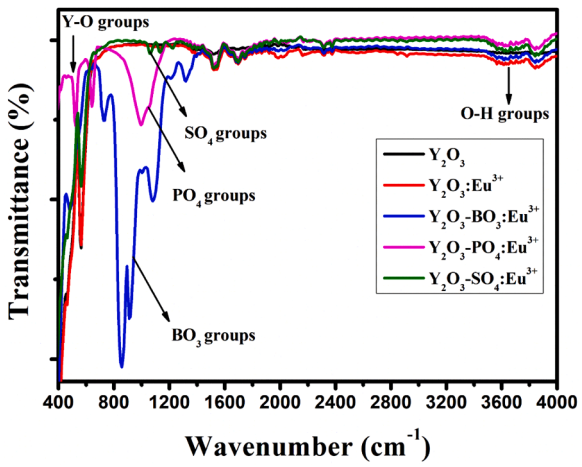

Fig. 7. FT-IR spectra of Y_2O_3: Eu^{3+}, Y_2O_3-BO_3: Eu^{3+}, Y_2O_3-PO_4: Eu^{3+} and Y_2O_3-SO_4: Eu^{3+} phosphors.

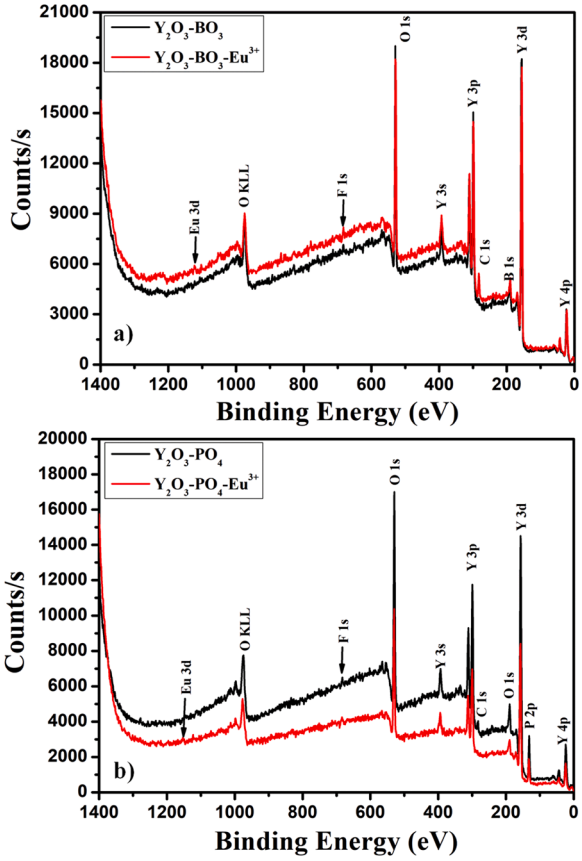

Fig. 8. XPS survey scan spectra of a) the Y_2O_3-BO_3 and Y_2O_3-BO_3:Eu^{3+} and b) the Y_2O_3-PO_4 and Y_2O_3-PO_4:Eu^{3+} phosphors.

and 157.51 eV respectively [39]. Similarly, the Gaussian triplet configuration of the O 1 s profile reflects the presence of oxygen through Eu-O, Y-O and B-O bonding groups positioned at binding energies of 528.79, 530.85, and 532.05 eV respectively [40,38] Fig. 10(a–d) shows high-resolution XPS spectra of Y 3d, P 2p, O 1 s c 1 s, and Eu 3d of the Y_2O_3-PO_4 and Y_2O_3-PO_4:Eu^{3+} nano phosphors. The element Y 3d has an oxidation state of +3 corresponding to a binding energy of 158.41 eV [35], and the element P 2p has a pentavalent oxidation state of +5 corresponding to a binding energy of 133.79 eV [41] and the element O 1 s has an oxidation state of −2 corresponding to a binding energy of 531.50 eV [37]. Furthermore, Eu 3d has an oxidation state of +3 with doublet spin-orbit coupling states of $3d_{3/2}$ and $3d_{5/2}$ corresponding to a binding energy of 1133.87 and 1154.62 eV respectively [38]. The additional peaks positioned at 1124.10 eV and 1155.24 eV are attributed to the presence of the +3 state of Eu atoms [38]. The inset figures of Fig. 10(a) and (c) shows the Gaussian fitting of the peaks for Y 3d and O 1 s profiles, respectively [39,40,38]. The doublet deconvoluted peaks of Y 3d indicates that the doublet spin-orbit coupling states at $3d_{3/2}$ and $3d_{5/2}$ correspond to a binding energy of 159.32 eV and 157.35 eV respectively [39]. Similarly, the Gaussian triplet configuration of the O 1 s profile reflects the presence of oxygen through Eu-O, Y-O, and P-O bonding groups with binding energies of 528.95, 530.49, and 531.55 eV respectively [40,38].

3.5. UV–VIS and band gap measurements

Fig. 11 shows the UV–VIS reflection spectra of the Y_2O_3: Eu^{3+}, Y_2O_3-BO_3: Eu^{3+}, Y_2O_3-PO_4: Eu^{3+} and Y_2O_3-SO_4: Eu^{3+} phosphors in the wavelength spectral range of 200–800 nm. From the figure it is observed that there are greater absorption signals in the UV region around 340 nm wavelength, whereby the anionic group materials have a greater absorption compared to the un-doped materials. This spectra shows, no traces of Eu^{3+} absorption bands for Eu^{3+} doped material because of low concentration of Eu^{3+} ions (1 mol%) [42,43]. The spectral bands in the profile clearly indicate that the absorption bands were blue-shifted, which corresponds to increases in band gap values over the addition of anionic group systems [44,45]. From a reflectance spectrum, the optical bandgap can be estimated by using the Kubelka-Munk function as a function of photon energy *hν* [46,47]. The optical band gap is an important feature of an any material that determine its application in various fields [48]. The K-M function relates the absorption coefficient, the scattering coefficient, of the Diffuse Reflectance spectra (DRS) in the format:

$$\mathbf{F}(\mathbf{R}_\infty) = \frac{(1-\mathbf{R}_\infty)^2}{2\mathbf{R}_\infty} = \frac{\mathbf{K}}{\mathbf{S}} \tag{3}$$

Therefore, the Optical gap energy and the absorption coefficient can be related by the Tauc relation [48]:

$$(\alpha \mathbf{h}\nu) = \mathbf{C}_0(\mathbf{h}\nu - \mathbf{E}_g)^{\mathbf{n}} \tag{4}$$

From the plot of $[F(R_\infty).h\nu]^2$ against photon energy hv, the band gap energy of a materials can be extrapolated by a linear fit to the $[F(R_\infty).h\nu]^2$ =0 model.

Fig. 12 shows the plots of $F(R_\infty)$ as a function of photon energy hν for individual band transitions with n = ½ or 2. The extrapolation of the linear line to intercept the X-axis at $F(R_\infty) = 0$, gives the bandgap values of the respective materials. All estimated bandgap values are tabulated in Table 4. From the table it is observed that the band gap value for the Y_2O_3 host materials have increased after doping of Eu^{3+} ions, this phenomenon is described by the Burstein-Moss effect [49]. The insert chart diagram in the table displays the variation of the bandgap absorption edge, resulting from the incorporation of different anionic group systems. The absorption edge abruptly increased for the Y_2O_3: Eu^{3+} phosphors when substituted with the BO_3^{3-} and PO_4^{2-} anionic group systems, whereas the absorption edge decreased for substitution of SO_4^{2-} groups [24,50]. This is mainly due to the structural changes that occurred in the cubic structures for Y_2O_3-BO_3: Eu^{3+} (hexagonal) and Y_2O_3-PO_4: Eu^{3+} (tetragonal) phosphors.

3.6. Photoluminescence excitation and emission spectra measurements

Fig. 13(a) shows the PL excitation spectra of the Y_2O_3: Eu^{3+}, Y_2O_3-BO_3: Eu^{3+}, Y_2O_3-PO_4: Eu^{3+} and Y_2O_3-SO_4: Eu^{3+} phosphors in the wavelength range of 300–560 nm by monitoring the emission band at 615 nm. These spectra consist of six characteristic excitation peaks

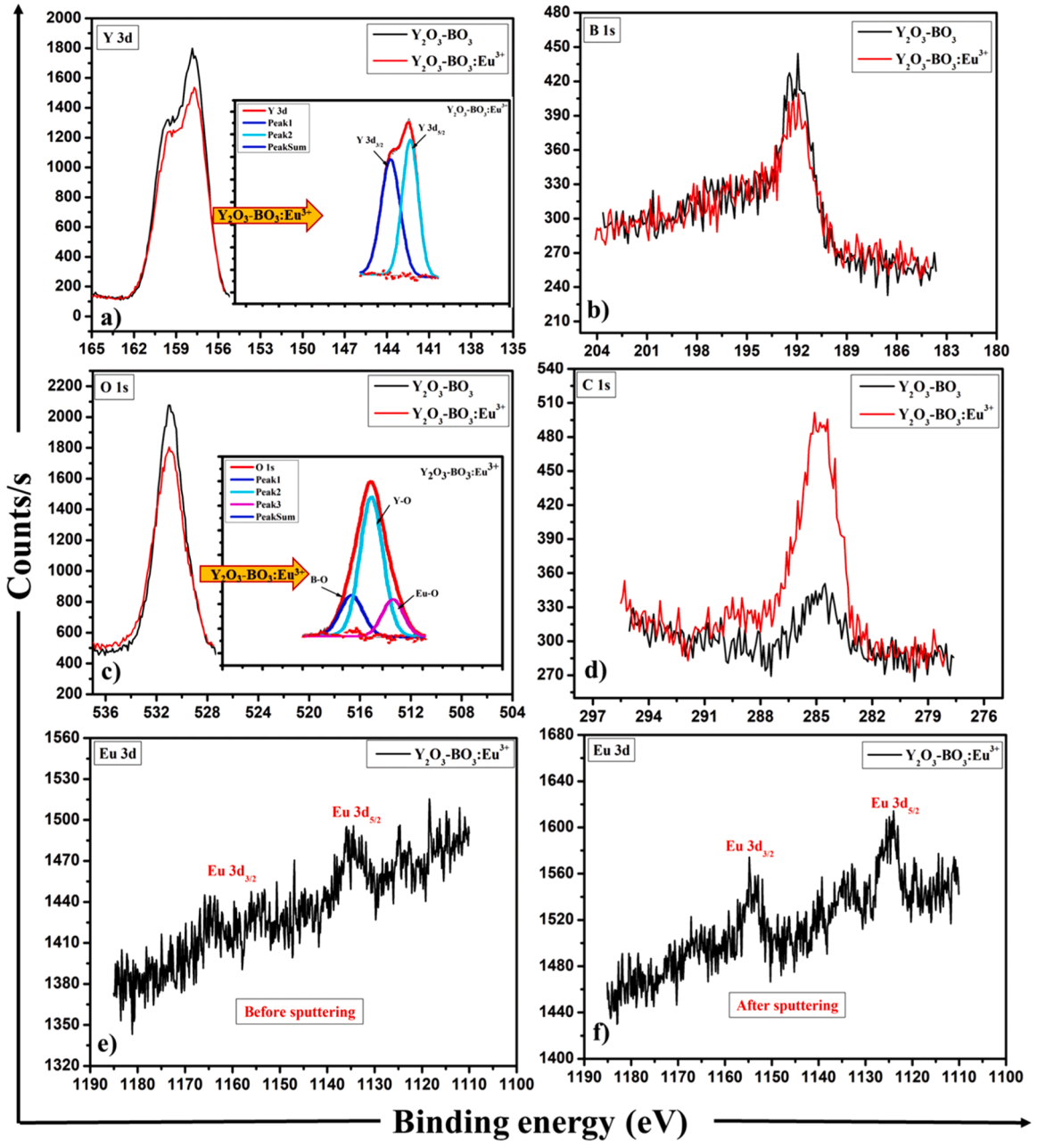

Fig. 9. The high-resolution XPS scan spectra of (a) Y 3d (b) B 1 s (c) O 1 s (d) C 1 s (e),(f)Eu 3d for the Y_2O_3-BO_3 and Y_2O_3-BO_3: Eu^{3+}phosphors.

which are attributed to the $4f_6 \rightarrow 4f_6$ intra-configurational bands arising due to the transitions from the ground state $^7F_0$ to the various excited states of Eu^{3+} ions such as ^5D_J (where $J = 0$–3) and $^5L_6$ [51,52]. These excitation bands positioned at 361, 395, 464, 524, and 532 nm are due to the $^7F_0 \rightarrow$ $^5D_4$, $^5L_6$, $^5D_2$, $^5D_1$, and $^5D_1$ transitions of Eu^{3+} ions, respectively. Among all these band transitions, the high-intensity band observed at 395 nm, was used to measure the PL emission spectra of the prepared materials.

Fig. 13(b) shows the emission spectra of the Y_2O_3: Eu^{3+}, Y_2O_3-BO_3: Eu^{3+}, Y_2O_3-PO_4: Eu^{3+} and Y_2O_3-SO_4: Eu^{3+} phosphors in the wavelength range of 550–720 nm, which were recorded using the excitation wavelength of 395 nm ($^7F_0 \rightarrow ^5L_6$). The six characteristic emission bands found in the spectra are attributed to the $^5D_0 \rightarrow ^7F_J$ ($J = 0$–4) transitions of Eu^{3+} ions [53]. Among all these transitions, the highest emission band was noticed at 615 nm, which is due to the electric dipole transitions of Eu^{3+} ions in the red color region [54]. This spectrum indicates that the pure Y_2O_3 has shown a very low-intensity emission band, and the subsequent addition of anions has had a remarkable influence on the luminescence properties of this pure Y_2O_3 phosphor (100 times better). This can be described by the high intensity absorption/excitation of the UV light for the Y_2O_3: Eu^{3+}, Y_2O_3-BO_3: Eu^{3+}, Y_2O_3-PO_4: Eu^{3+} and Y_2O_3-SO_4: Eu^{3+} phosphors due to the anionic substitutions. This creates more efficient UV light absorption in Y_2O_3-BO_3: Eu^{3+}, Y_2O_3-PO_4: Eu^{3+}, and Y_2O_3-SO_4: Eu^{3+} phosphors, thereby resulting in enhanced Eu^{3+} ion emissions, [50, 55,56] as shown in Fig. 13(b). A comparison of all the emission profiles indicates that the Y_2O_3-BO_3 phosphors produced the highest red-emitting color, followed by the Y_2O_3-PO_4 and Y_2O_3-SO_4 phosphor materials, respectively with the trend of Y_2O_3-BO_3>Y_2O_3-PO_4>Y_2O_3-SO_4. These results suggest that the red-emitting Y_2O_3-BO_3 phosphor is a potential candidate for w-LEDs applications [57].

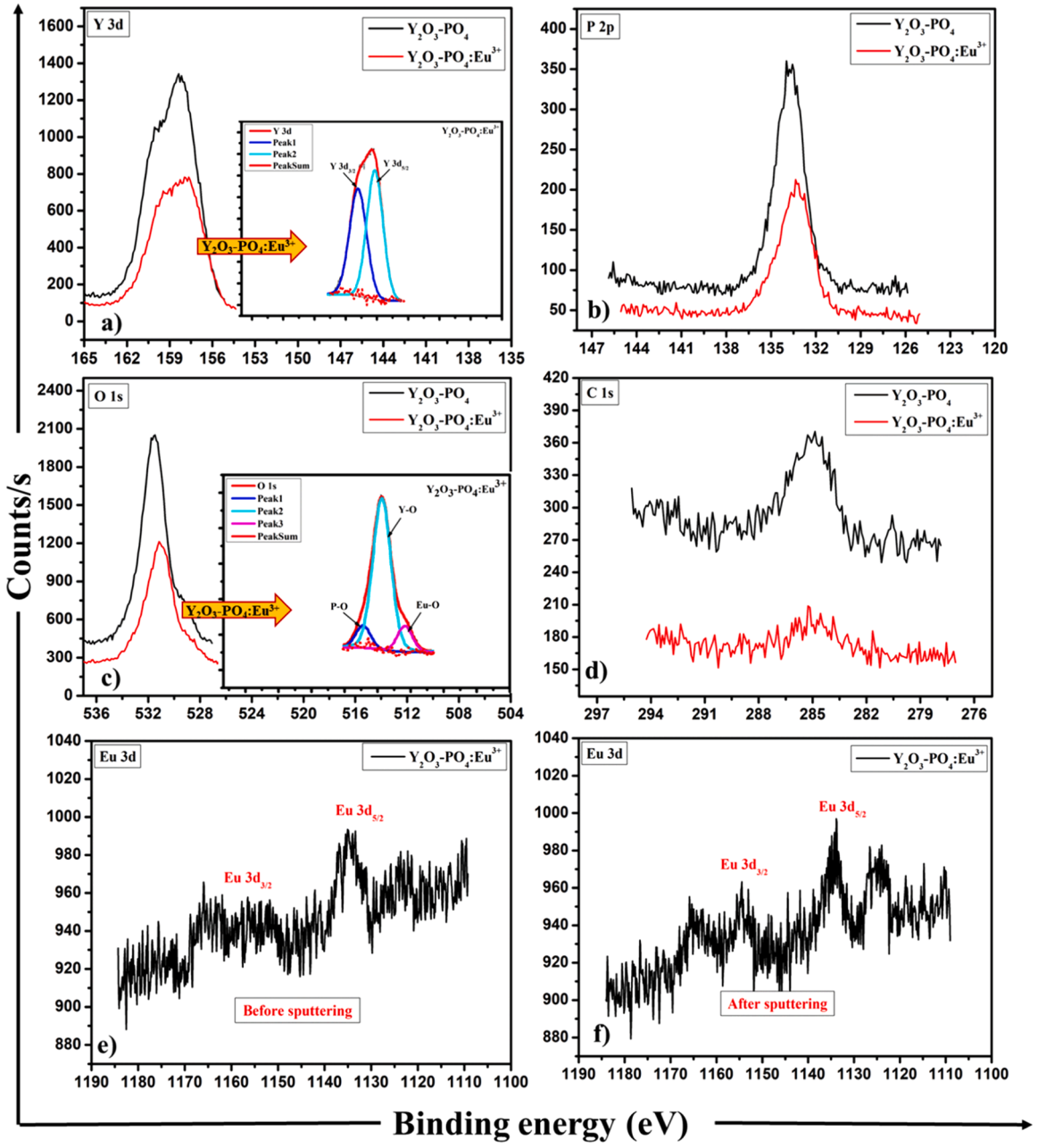

Fig. 10. . The high-resolution XPS scan spectra of (a) Y 3d (b) P 2p (c) O 1 s (d) C 1 s (e),(f)Eu 3d for the Y_2O_3-PO_4 and Y_2O_3-PO_4: Eu^{3+}phosphors.

3.7. Quantum yield

The quantum yield of the Eu^{3+} ion luminescence in the Y_2O_3-AG: Eu^{3+} nanophosphors were determined from the plots as shown in Fig. 14 (a–d). These spectra were divided into two regions: reflection of light from the external source at 397 nm and color emission from the phosphors at longer wavelengths as plotted and shown as a magnified insert plot in Fig. 14(a–d). The response of a reflective Spectralon standard is given by Curve 1 compared to the sample of Curve 2 in each case. The number of photons absorbed can be estimated by subtracting the curves and integrating the photon distribution near the excitation wavelength of 397 nm [58]. The quantum yield (QY) of the prepared materials were estimated using the data provided in the photon distribution curves, as reported in our previous paper [24]. The QY values for the Y_2O_3:Eu^{3+}, and Y_2O_3-AG: Eu^{3+} nanophosphors were determined to be 2.4, 17, 11 and 15 % respectively. These QY values are good agreement with previously reported values and were found to be enhanced after different anionic group substitution into the Y_2O_3:Eu^{3+} phosphors [59].

3.8. Lifetime decay measurements

Fig. 15 shows the lifetime decay profile of the Y_2O_3: Eu^{3+}, Y_2O_3-BO_3: Eu^{3+}, Y_2O_3-PO_4: Eu^{3+} and Y_2O_3-SO_4: Eu^{3+} phosphors, using 395 nm and 615 nm excitation and emission wavelengths, respectively. The lifetime profile of the phosphors were well-matched to the non-exponential function of the equation [60].

$$I = I_0 + A_1\exp\left(\frac{-t}{\tau_1}\right) + A_2\exp\left(\frac{-t}{\tau_2}\right) \quad (5)$$

where I is the emission intensity. Fast and slow lifetimes are represented by τ_1 and τ_2, respectively. In addition to that the fitting constants A_1 and A_2 are evaluated. The average lifetime decay from excitation to ground state is given by the equation, [60]

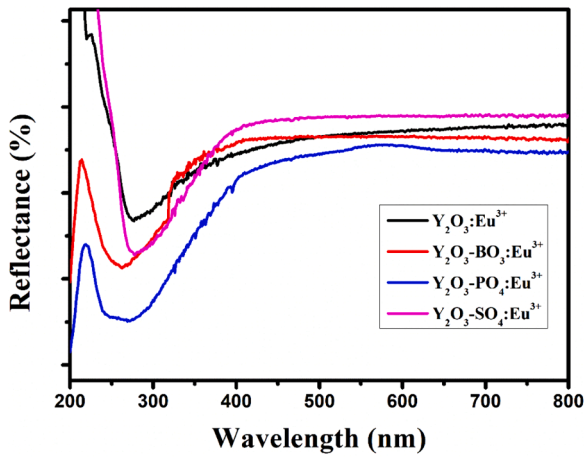

Fig. 11. UV–Vis DRS spectra of Y_2O_3: Eu^{3+}, Y_2O_3-BO_3: Eu^{3+}, Y_2O_3-PO_4: Eu^{3+} and Y_2O_3-SO_4: Eu^{3+} phosphors.

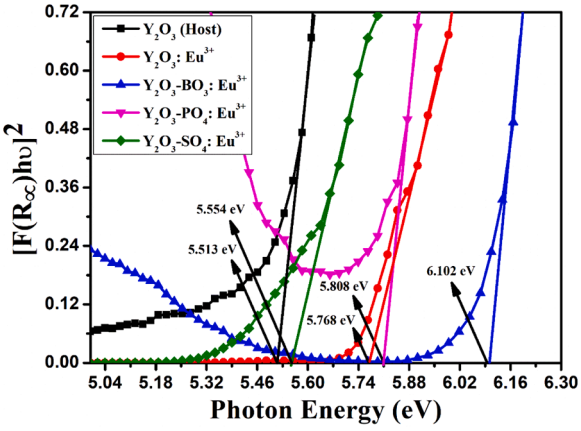

Fig. 12. Optical bandgap calculations of Y_2O_3, Y_2O_3: Eu^{3+}, Y_2O_3-BO_3: Eu^{3+}, Y_2O_3-PO_4: Eu^{3+} and Y_2O_3-SO_4: Eu^{3+} phosphors. The line represents the best linear fit to determine the energy band gaps.

$$\tau_{avg} = \frac{A_1\tau_1^2 + A_2\tau_2^2}{A_1\tau_1 + A_2\tau_2} \tag{6}$$

The average lifetime decay for Y_2O_3: Eu^{3+}, Y_2O_3-BO_3: Eu^{3+}, Y_2O_3-PO_4: Eu^{3+} and Y_2O_3-SO_4: Eu^{3+} phosphors are tabulated in Table 5. From this table, it is observed that the lifetime decay of Y_2O_3: Eu^{3+}, Y_2O_3-BO_3: Eu^{3+}, Y_2O_3-PO_4: Eu^{3+} have similar values of 1.705, 1.737, 1.757 milliseconds respectively while that of Y_2O_3-SO_4: Eu^{3+} was much lower decay time of at 1.192 milliseconds. This behavior may be attributed to the occurrence of traps created within the bandgap of the host materials [61]. The lower lifetime decay for the Y_2O_3-SO_4: Eu^{3+} based materials is due to shallow traps [62], which was also evidenced directly from the

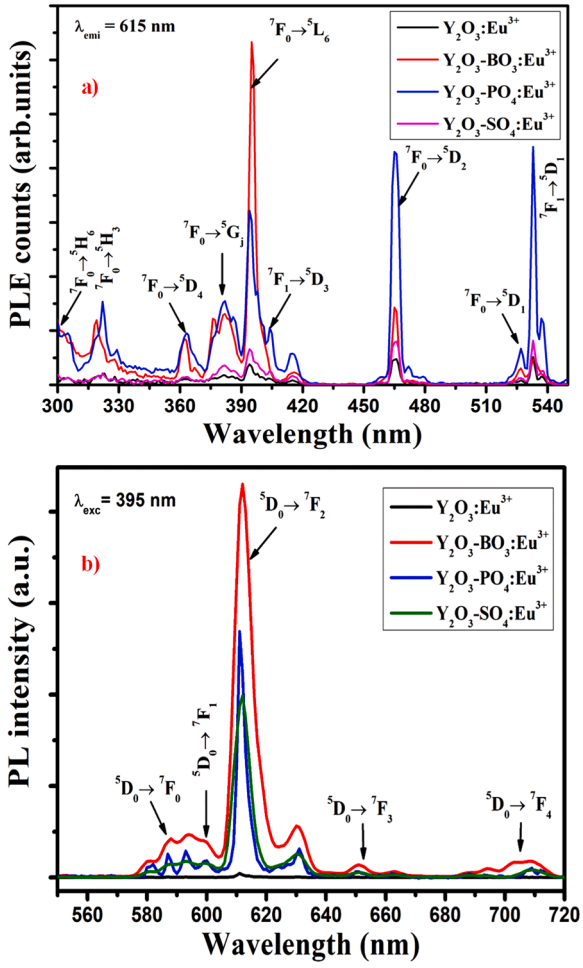

Fig 13. (a) Photoluminescence excitation and (b) Photoluminescence emission spectra of Y_2O_3: Eu^{3+}, Y_2O_3-BO_3: Eu^{3+}, Y_2O_3-PO_4: Eu^{3+} and Y_2O_3-SO_4: Eu^{3+} phosphors.

Table 4
Optical bandgap values of the Y_2O_3: Eu^{3+}, Y_2O_3-BO_3: Eu^{3+}, Y_2O_3-PO_4: Eu^{3+} and Y_2O_3-SO_4: Eu^{3+} phosphors. Insert chart represents the schematic diagram of absorption edge variation.

S. No	Prepared Sample	Band gap (eV)
1	Y_2O_3 (Cubic)	5.513
2	Y_2O_3: Eu^{3+} (Cubic)	5.768
3	Y_2O_3-BO_3: Eu^{3+} (Hexagonal)	6.102
4	Y_2O_3-PO_4: Eu^{3+} (Tetragonal)	5.808
5	Y_2O_3-SO_4: Eu^{3+} (Cubic)	5.544

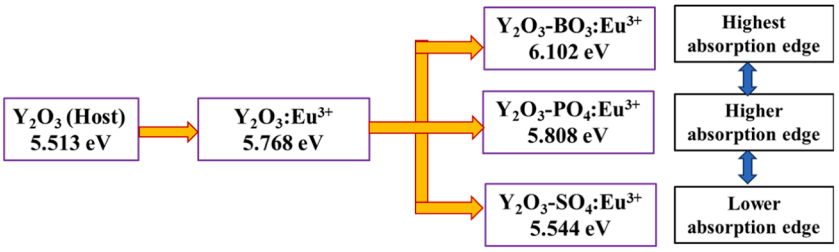

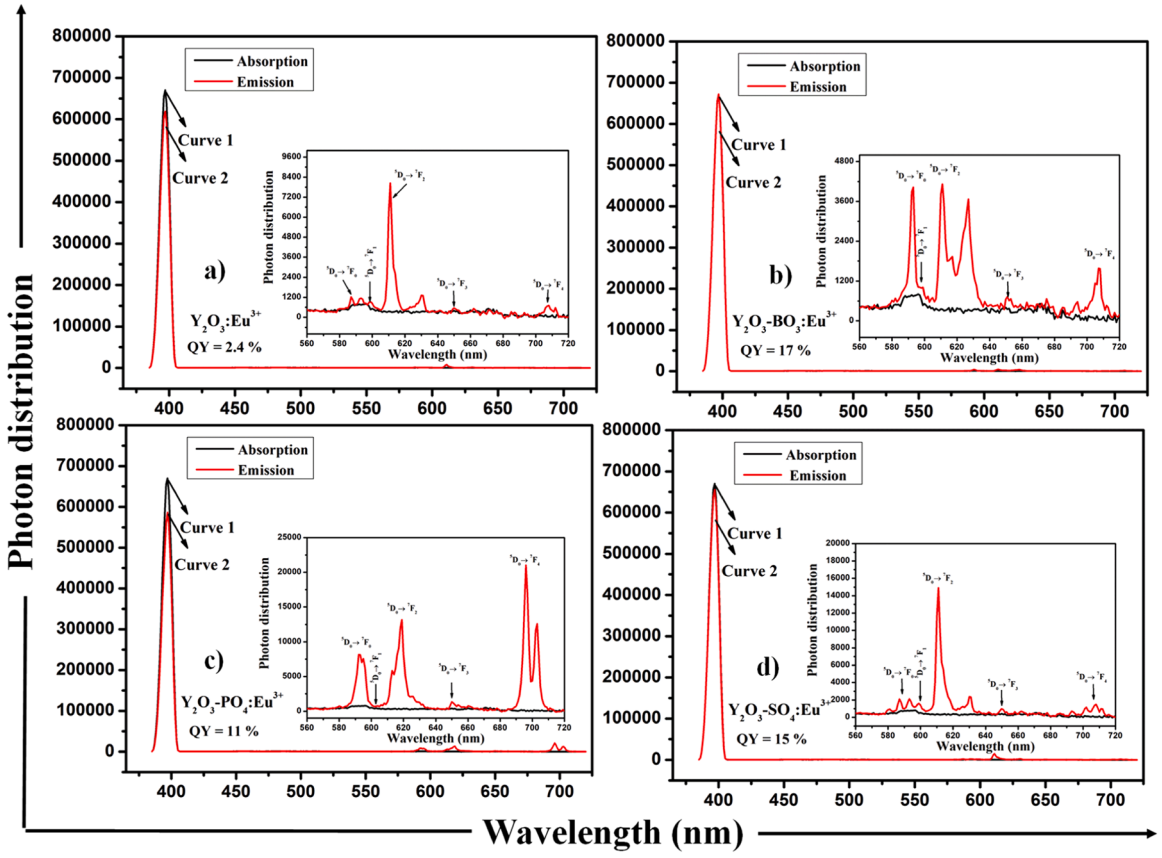

Fig. 14. Spectral power distribution of Eu^{3+} ion in a) Y_2O_3: Eu^{3+} b) Y_2O_3-BO_3: Eu^{3+} c) Y_2O_3-PO_4: Eu^{3+} and d) Y_2O_3-SO_4: Eu^{3+} phosphors.

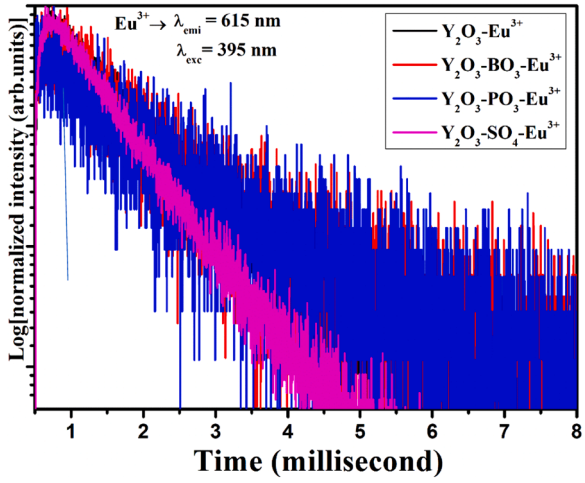

Fig 15. Lifetime decay profiles of Y_2O_3: Eu^{3+}, Y_2O_3-BO_3: Eu^{3+}, Y_2O_3-PO_4: Eu^{3+} and Y_2O_3-SO_4: Eu^{3+} phosphors.

Table 5
Average lifetime decay values of the Y_2O_3: Eu^{3+}, Y_2O_3-BO_3: Eu^{3+}, Y_2O_3-PO_4: Eu^{3+} and Y_2O_3-SO_4: Eu^{3+} phosphors.

S.No	Sample	Lifetime decay (ms)
1	Y_2O_3: Eu^{3+}	1.705
2	Y_2O_3-BO_3: Eu^{3+}	1.737
3	Y_2O_3-PO_4: Eu^{3+}	1.757
4	Y_2O_3-SO_4: Eu^{3+}	1.193

decay profile pattern and the extra hump gap calculations profile.

3.9. CIE color coordinates

Fig. 16 displays the Commission Internationale de l'Elcairage (CIE) of Y_2O_3: Eu^{3+}, Y_2O_3-BO_3: Eu^{3+}, Y_2O_3-PO_4: Eu^{3+} and Y_2O_3-SO_4: Eu^{3+} phosphors. The calculated CIE coordinate values were tabulated in the insert figure of Fig. 16. All the values were lying in the red color region of the chromaticity diagram. These results verified that the prepared phosphor materials are potential red emitting candidates for white LEDs applications.

4. Conclusions

In the present work, the combustion method was used to synthesize Y_2O_3, Y_2O_3-AG: Eu^{3+} nanophosphors. XRPD analysis confirmed the impact of the substitution of different the anionic groups on the cubic structure of the Y_2O_3: Eu^{3+} phosphors resulting in new structures such as hexagonal and tetragonal structures for the Y_2O_3-BO_3 and Y_2O_3-PO_4 phosphors, respectively. However the Y_2O_3-SO_4 cubic structure was not transformed. The SEM analysis revealed a wide particle size distribution from compactness to agglomeration. The FT-IR and XPS results confirmed the presence of the functional groups and oxidation states of all elements present. To report the impact of the anionic group substitutions on the optical properties, the bandgaps of the prepared materials were obtained. The anionic group based Y_2O_3 materials, exhibited significant changes in the PL profiles in comparison to the pure Y_2O_3:Eu^{3+} phosphors. The PL results revealed that the Y_2O_3-AG: Eu^{3+} phosphor materials can be effectively excited in the UV range to emit more efficient red light with improved quantum efficiency. The CIE chromaticity diagram indicated that the color coordinates of the respective anionic groups were in the red color region. From this

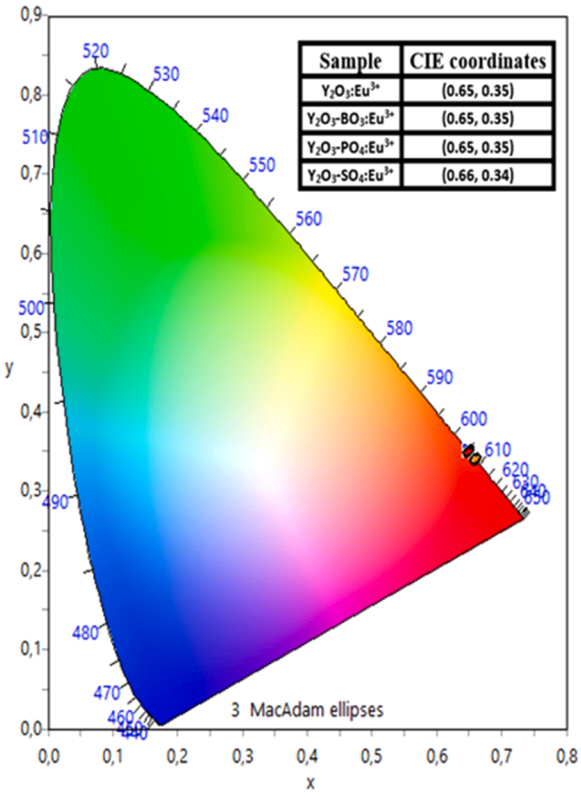

Fig 16. CIE diagram of Y_2O_3: Eu^{3+}, Y_2O_3-BO_3: Eu^{3+}, Y_2O_3-PO_4: Eu^{3+} and Y_2O_3-SO_4: Eu^{3+} phosphors.

investigation, amongst all prepared materials, Y_2O_3-BO_3:Eu^{3+} produced the highest red color emission, making it an ideal candidate for high intensity red-emitting phosphor materials in W-LEDs applications.

CRediT authorship contribution statement

T.G. Mathe: Writing – original draft, Conceptualization, Methodology, Software. **A. Balakrishna:** Resources, Validation, Conceptualization, Visualization, Writing – review & editing, Supervision. **M.A. Mamo:** Resources, Software, Conceptualization, Writing – review & editing. **O.M. Ntwaeaborwa:** Software, Validation, Conceptualization, Supervision, Writing – review & editing. **R.E. Kroon:** Resources, Software, Conceptualization, Writing – review & editing. **E. Coetsee:** Resources, Conceptualization, Validation, Writing – review & editing. **H.C. Swart:** Resources, Conceptualization, Validation, Writing – review & editing. **L. Reddy:** Resources, Validation, Conceptualization, Visualization, Writing – review & editing, Supervision.

Declaration of Competing Interest

The authors declare that they have no known competing financial interests or personal relationships that could have appeared to influence the work reported in this paper.

Data availability

Data will be made available on request.

Acknowledgments

The South African National Nanoscience Postgraduate Teaching and Training Platform (NNPTTP) of the Department of Science and Technology support this work financially. This research is also based on the research supported in part by the National Research Foundation of South Africa (Grant Number 84415 H.C. Swart, UFS).

References

[1] C.M. Nandanwar, N.S. Kokode, A.N. Yerpude, S.J. Dhoble, Luminescence properties of $BiPO_4$:Ln (Ln = Dy^{3+}, Tb^{3+} and Sm^{3+}) orthophosphate phosphors for near-UV-based solid-state lighting, Bull. Mater. Sci. 46 (2023) 51.
[2] M.D. Mehare, C.M. Mehare, H.C. Swart, S.J. Dhoble, Recent development in color tunable phosphors: a review, Prog. Mater Sci. (133) (2023), 101067.
[3] J. Li, Y. Zheng, H. Zhang, H. Li, T. Yang, Y. Xiang, J. Zhang, J. Zhu, Microwave-assisted synthesis and thermally stable red fluorescence of $Ba_3(ZnB_5O_{10})PO_4$:Eu^{3+} solid solution, J. Solid State Chem. 322 (2023), 124000.
[4] H. Kong, G. Jia, H. Li, Z. Meng, N. Zhang, C. Zhang, Deep blue, cyan, orange-red, and white multicolor emissions generated by Bi^{3+}/Eu^{3+} activated $KBaYSi_2O_7$ luminescent materials for white light-emitting diodes, Ceram. Int. 49 (10) (2023) 15320–15332.
[5] R. Kanga, Y. Wang, A novel high efficiency emission-tunable solid solution luminescent material with non-concentration-quenching and excellent thermal stability, J. Mater. Chem. C 10 (2022) 16884–16892.
[6] B. Lin, Y. Zhang, Z. Zhao, H. Zhao, J. Yu, Tunable red/blue emitting of $Ca_5(PO_4)_3F$: Eu^{2+}, Eu^{3+} and remote-excited color convertor for NUV-WLED, Opt. Mater. 137 (2023), 113609. Amst.
[7] D. Tu, Y. Liang, R. Liu, D. Li, Eu/Tb ions co-doped white light luminescence Y_2O_3 phosphors, J. Lumin. 131 (12) (2011) 2569–2573.
[8] W.C. Chien, Synthesis of Y_2O_3:Eu phosphors by bicontinuous cubic phase process, J. Cryst. Growth 290 (2) (2006) 554–559.
[9] J.B. Pendry, Photonic band structures, J. Mod. Opt. 41 (2) (1994) 209–229.
[10] L. Sandhya Kumari, P. Prabhakar Rao, A. Narayana Pillai Radhakrishnan, V. James, S. Sameera, P. Koshy, Brilliant yellow color and enhanced NIR reflectance of monoclinic $BiVO_4$ through distortion in VO_4^{3-} tetrahedra, Sol. Energy Mater. Sol. Cells 112 (2013) 134–143.
[11] D. Kumar, M. Sharma, O.P. Pandey, Effect of co-doping metal ions (Li^+, Na^+ and K^+) on the structural and photoluminescent properties of nano-sized Y_2O_3:Eu^{3+} synthesized by co-precipitation method, Opt. Mater 36 (7) (2014) 1131–1138.
[12] A. Dwivedi, M. Srivastava, A. Dwivedi, A. Srivastava, A. Mishra, S.K. Srivastava, Synthesis and enhanced photoluminescence properties of red emitting divalent ion (Ca^{2+}) doped Eu:Y_2O_3 nanophosphors for optoelectronic applications, J. Rare Earths 40 (8) (2022) 1187–1198.
[13] A. Yousif, B.H. Abas, S. Som, N.J. Shivaramu, H.C. Swart, Structural and luminescence properties of Y_2O_3:Eu^{3+}red phosphor by incorporation of Ga^{3+} and Bi^{3+}ions, Mater. Res. Bull. 124 (2020), 110752.
[14] R.S. Ukare, G.D. Zade, B.D Prasad Raju, S.J. Dhoble, Effect of Li^+ and Zn^{2+} co-doping on PL properties of Y_2O_3:Eu^{3+} phosphor, Optik 127 (4) (2016) 1871–1878.
[15] D. Wang, S. Tie, X. Wan, White light emitting from YVO_4/Y_2O_3:Eu^{3+},Bi^{3+} composite phosphors for UV light-emitting diodes, Ceram. Int. 41 (6) (2015) 7766–7772.
[16] I. Gupta, S. Singh, S. Bhagwan, D. Singh, Rare earth (RE) doped phosphors and their emerging applications: a review, Ceram. Int. 47 (14) (2021) 19282–19303.
[17] E.L.M. Bouabdalli, N. Gaumer, S. Touhtouh, Structural, optical behavior and Judd-Ofelt analysis of europium-doped silicophosphate glasses for red-emitting device applications, J. Lumin. 256 (2023), 119640.
[18] Q. Zeng, W. He, N. Zhang, D. Guo, Insight into luminescence properties of Li^+ co-doped Sr_2SnO_4:Eu^{3+} phosphors by co-precipitation assisted hydrothermal synthesis, J. Lumin. 253 (2023), 119452.
[19] Y. Tao, L. Zeng, Hu Zhou, J. Zeng, W. Wang, G. Liu, Y. Dai, J. Yu, T. Jianfeng, Fluorescent Ca^{2+}-doped $LaVO_4$:Eu^{3+} nanocrystals featuring highly sensitive detecting Cu^{2+} ions, Opt. Mater. 132 (2022), 112766.
[20] E. Rai, R.S. Yadav, D. Kumar, A.K. Singh, V.J. Fulari, S.B. Rai, Improved photoluminescence in Eu^{3+} doped $LaVO_4$ phosphor via co-doping of Li^+/Ca^{2+} ions, J. Lumin. 241 (2022), 118519.
[21] H. Zhou, K. Zhu, J. Wang, J. Qiu, L. Yue, L.G. Wang, L. Ye, Effects of Yb^{3+} concentration on up-conversion luminescence and temperature sensing characteristics of Tm^{3+}/Yb^{3+}:Y_2O_3 phosphors, J. Alloys Compd. 918 (2022), 165674.
[22] I. Halevy, R. Carmon, M.L. Winterrose, O. Yeheskel, E. Tiferet, S. Ghose, J. Phys. Conf. Ser. 215 (2010), 012003.
[23] R.E. Kroon, Nanoscience and the Scherrer equation versus the 'Scherrer–Gottingen equation', S. Afr. J. Sci. 109 (5/6) (2013) 1–2, https://doi.org/10.1590/sajs.2013/a0019. Art. #a0019, pages.
[24] A. Balakrishna, H.C. Swart, R. Ramaraghavulu, A.K. Bedyal, R.E. Kroon, O. M. Ntwaeaborwa, Structural evolution induced by substitution of designated molybdate sites (MoO_4^{-2}) with different anionic groups (BO_3^{-3}, PO_4^{-3} and SO_4^{-2}) in $CaMoO_4$:Sm^{3+} phosphors-A study on color tunable luminescent properties, J. Alloys Compd. 727 (2017) 224–237.
[25] N.J. Shivaramu, B.N. Lakshminarasappa, K.R. Nagabhushana, F. Singh, Synthesis characterization and luminescence studies of gamma irradiated nanocrystalline yttrium oxide, Spectrochim. Acta Part A (154) (2016) 220–231.
[26] Y.P. Fu, S.B. Wen, C.S. Hsu, Preparation and characterization of $Y_3Al_5O_{12}$:Ce and Y_2O_3:Eu phosphors powders by combustion process, J. Alloys Compd. 458 (1–2) (2008) 318–322.

[27] R.S. Yadav, Energy transfer induced color tunable photoluminescence in Tb^{3+}/Sm^{3+} co-doped Y_2O_3 nano-phosphor for warm white LEDs, J. Alloys Compd. 931 (2023), 167579.

[28] G. Blasse, Energy transfer in oxidic phosphors, Phys. Lett. A 28 (6) (1968) 444–445.

[29] R.D. Shannon, Revised effective ionic radii and systematic studies of interatomic distances in halides and chalcogenides, Acta Cryst. A 32 (1976) 751–767, https://doi.org/10.1107/S0567739476001551.

[30] C. Wen, R. Zhou, Z. Qiu, J. Yang, X. Zhang, H. Xu, Fabrication and surface hydrophobic modification of $Y_2O_3:Eu^{3+}$ phosphors, React. Chem. Eng. 8 (2023) 871–880.

[31] M.L.A. Letswalo, L. Reddy, A. Balakrishna, H.C. Swart, O.M. Ntwaeaborwa, Influence of SO_4^{2-} anionic group substitution on the enhanced photoluminescence behaviour of red emitting $CaMoO_4:Eu^{3+}$ phosphor, J. Alloys Compd. 854 (2021), 157022.

[32] P. Bhattacharyya, S. Sahoo, A.H. Seikh, S.M.A.K Mohammed, A. Sarkar, Nabeel Alharthi, Synthesis, characterization and optical property study of BCNO and BCN related nanopowder, Diam. Relat. Mater. 92 (2019) 235–241.

[33] A.I. Kostyukov, V.N. Panchenko, A.A. Nashivochnikov, M.I. Rakhmanova, S. V. Cherepanova, E.A. Suprun, O. Antonova, High quantum yield of red-emitting Eu^{3+} doped nanophosphor based on monoclinic Y_2O_3, Ceram. Int. 49 (2023) 41158–41166.

[34] M. Shi, H. Zhao, J. Zou, B. Yang, Y. Li, Z. Wang, C. Chang, W. Li, Preparation and characterization of a new long afterglow phosphor $CaSnO_3$: Yb^{3+}, J. Mater. Sci. Mater. Electron. 28 (2017) 10067–10072.

[35] N.J. Shivaramu, B.N. Lakshminarasappa, E. Coetsee, R.E. Kroon, H.C. Swart, Structural, thermoluminescence and optical properties of Nd^{3+} doped Y_2O_3 nanophosphor for dosimeter and optoelectronics applications, Mater. Res. Bull. (161) (2023), 112153.

[36] SS. Pitale, I.M. Nagpure, V. Kumar, O.M. Ntwaeaborwa, J.J. Terblans, H.C. Swart, Investigations on the low voltage cathodoluminescence stability and surface chemical behaviour using Auger and X-ray photoelectron spectroscopy on $LiSrBO_3$: Sm^{3+} phosphor, Mater. Res. Bull. 46 (7) (2011) 987–994.

[37] W.L. Lian, P. Liang, Z.H. Liu, Controllable hydrothermal synthesis and morphology evolution of $Zn_4B_6O_{13}$:Tb/Eu phosphors with tunable luminescent properties, Adv. Powder Technol. 31 (4) (2020) 1633–1642.

[38] J. Bi, L. Sun, Q. Wei, K. Zhang, L. Zhu, S. Wei, D. Liao, J. Sun, Rapid ultrasonic-microwave assisted synthesis of Eu^{3+} doped Y_2O_3 nanophosphors with enhanced luminescence properties, J. Mater. Res. Technol. 9 (5) (2020) 9523–9530.

[39] E. Lee, J.J. Terblans, H.C. Swart, The effect of pH on the luminescence properties of Y_2O_3:Bi phosphor powders synthesised using co-precipitation, Vac. Vol. 157 (2018) 237–242.

[40] I. Charak, M. Manhas, A.K. Bedyal, S. Singh, A. Srivastava, H.C. Swart, V. Kumar, Structural and spectral studies of highly pure red-emitting $Ca_3B_2O_6:Eu^{3+}$ phosphors for white light emitting diodes, J. Alloys Compd. 869 (2021), 159363.

[41] A.P. Sefage, M.A. Mamo, P.L. Masiteng, A. Balakrishna, E. Coetsee, H.C. Swart, L. Reddy, The concentration effect of Ce^{3+} ions on the photoluminescence properties of the host sensitized $NaMPO_4$-Ce^{3+} (M = Mg and Ca) phosphors via solid-state reaction method, Phys. B 647 (2022), 414383.

[42] A.K. Parchur, A.I. Prasad, S.B. Rai, R. Tewari, R.K. Sahu, G.S. Okram, R.A. Singh, Raghumani Singh Ningthoujam; observation of intermediate bands in Eu^{3+} doped YPO_4 host: Li^+ ion effect and blue to pink light emitter, AIP Adv. 2 (3) (2012), 032119.

[43] A. George, S. Gopi, E. Sreeja, E.T. Krishnapriya, A.C. Saritha, C. Joseph, N. V. Unnikrishnan, P.R. Biju, Host sensitized tunable luminescence of single phase white light emitting $Ca_2Sb_2O_7:Eu^{3+}$ phosphors, J. Mater. Sci. Mater. Electron. 31 (2020) 423–434.

[44] C. Ren, X. Zhang, L. Zhou, Z. Lu, J. Lin, X. Xu, L. Li, X. Zhang, Y. Xue, F. Meng, J. Zhao, Chengchun Tang, Preparation optimization and spectral properties of BCNO phosphors with high quantum efficiency, J. Lumin. 153 (2014) 338–342.

[45] R.P. Moreira, L.H.C. Francisco, I.F. Costa, H.P. Barbosa, E.E.S. Teotonio, M.C.F. C. Felinto, O.L. Malta, H.F. Brito, Luminescence properties of $BaMO_4:Eu^{3+}$ (M: Mo or W) phosphors derived from co-precipitation reaction, J. Alloys Compd. 937 (2023), 168408.

[46] M. Picollo, M. Aceto, T. Vitorino, UV–Vis spectroscopy, Phys. Sci. Rev. 4 (4) (2019) 20180008.

[47] A.E. Morales, E.S. Mora, U. Pal, Use of diffuse reflectance spectroscopy for optical characterization of un-supported nanostructures, Rev. Mex. Fís. 53 (5) (2007) 18–22.

[48] S. Som, M. Chowdhury, S.K. Sharma, Band gap and trapping parameters of color tunable Yb^{3+}/Er^{3+} codoped Y_2O_3 upconversion phosphor synthesized by combustion route, J. Mater. Sci. 49 (2) (2014) 858–867.

[49] B. Vasanthi, N. Gopakumar, P.S. Anjana, Structural, optical and luminescence properties of $BaLaGa_3O_7$: xEu^{3+} ceramic phosphors, J. Lumin. 241 (2022), 118486.

[50] M.L.A. Letswalo, L. Reddy, A. Balakrishna, H.C. Swart, O.M. Ntwaeaborwa, The role of sulfate ions on distinctive defect emissions in ZnO:Ce3+ nanophosphors - a study on the application in color display systems, J. Lumin. 240 (2021), 118462.

[51] Y. Shi, R. Cui, X. Gong, C. Deng, A novel red phosphor $Ca_2YNbO_6:Eu^{3+}$ for WLEDs, Luminescence 37 (2022) 1343–1351.

[52] W. Geng, X. Zhou, A. Deng, W. Li, L. Zha, Charge transfer bands induced broad excitation Eu^{3+} red emission in a vanadium phosphate system for white light-emitting diodes, Inorg. Chem. 61 (2022) 8291–8297.

[53] S. Bhatia, R. Priya, D. Kumar, S. Upadhyay, O.P. Pandey, Structural and luminescence studies of titanium co-doped SrY_2O_4:Eu phosphors, Luminescence 37 (9) (2022) 1585.

[54] C. Kumari, J. Manam, S.K. Sharma, Strong red emission in double perovskite Sr_3LiSbO_6: Eu^{3+} phosphor with high color purity for solid-state lighting applications, Mater. Sci. Semicond. Process. 158 (2023), 107385.

[55] Y. Zhang, S. Shi, J. Gao, J. Zhou, Effects of $SO_4^{(2-)}$ or $SiO_3^{(2-)}$ doping on the photoluminescence of $NaEu(MoO_4)_2$ nanophosphors for light-emitting diodes, J. Nanosci. Nanotechnol. 10 (2010) 2156.

[56] W. Zhang, J. Li, Y. Wang, J. Long, K. Qiu, Synthesis and luminescence properties of $NaLa(MoO_4)_{2-x}AG_x$:Eu3+ (AG = SO_4^{2-}, BO_3^{3-}) red phosphors for white light emitting diodes, J. Alloys Compd. 635 (2015) 16–20.

[57] Tang, Z. and Jiang, L. and Yang, J. and Tang, J. and Wu, A., Synthesis of Eu^{3+}-activated $MRE(WO_4)_2$ red-emitting phosphors and application in near-ultraviolet-triggered white light-emitting diodes. Available at SSRN: https://ssrn.com/abstract=4048788 or 10.2139/ssrn.4048788.

[58] O.M. Ntwaeaborwa, S.J. Mofokeng, V. Kumar, E. Robin, Kroon, structural, optical and photoluminescence properties of Eu^{3+} doped ZnO nanoparticles, Spectrochim. Acta Part A 182 (2017) 42–49.

[59] M.T. Tran, N. Tu, N.V. Quang, D.H. Nguyen, L.T.H. Thu, D.Q. Trung, P.T. Huy, Excellent thermal stability and high quantum efficiency orange-red-emitting $AlPO_4:Eu^{3+}$ phosphors for WLED application, J. Alloys Compd. 853 (2021), 156941.

[60] C. Zou, N. Sun, W. Zhang, W. Li, Y. Huang, J. Fan, Effect of charge compensators on the luminescence enhancement of $Ca_2ZnSi_2O_7$: Sm^{3+} phosphors, J. Mater. Sci. Mater. Electron. 30 (18) (2019) 17412–17423.

[61] D. Komaraiah, E. Radha, J. James, N. Kalarikkal, J. Sivakumar, M.V. Ramana Reddy, R. Sayanna, Effect of particle size and dopant concentration on the Raman and the photoluminescence spectra of $TiO_2:Eu^{3+}$ nanophosphor thin films, J. Lumin. 211 (2019) 320–333.

[62] T. Dai, G. Ju, Y. Lv, Y. Jin, H. Wu, Y. Hu, Luminescence properties of novel dual-emission (UV/red) long afterglow phosphor $LiYGeO_4$: Eu^{3+}, J. Lumin. 237 (2021), 118193.